

Multimodal Characterization of Resin Embedded and Sliced Polymer Nanoparticles by Means of Tip-Enhanced Raman Spectroscopy and Force–Distance Curve Based Atomic Force Microscopy

Christiane Höppener,* Felix H. Schacher, and Volker Deckert

Understanding the property-function relation of nanoparticles in various application fields involves determining their physicochemical properties, which is still a remaining challenge to date. While a multitude of different characterization tools can be applied, these methods by themselves can only provide an incomplete picture. Therefore, novel analytical techniques are required, which can address both chemical functionality and provide structural information at the same time with high spatial resolution. This is possible by using tip-enhanced Raman spectroscopy (TERS), but due to its limited depth information, TERS is usually restricted to investigations of the nanoparticle surface. Here, TERS experiments are established on polystyrene nanoparticles (PS NPs) after resin embedding and microtome slicing. With that, unique access to their internal morphological features is gained, and thus, enables differentiation between information obtained for core- and shell-regions. Complementary information is obtained by means of transmission electron microscopy (TEM) and from force–distance curve based atomic force microscopy (FD-AFM). This multimodal approach achieves a high degree of discrimination between the resin and the polymers used for nanoparticle formulation. The high potential of TERS combined with advanced AFM spectroscopy tools to probe the mechanical properties is applied for quality control of the resin embedding procedure.


to their rich chemical and physical properties, which arise from the high variability of composition and morphologies.^[1] As such organic, inorganic, and hybrid nanoparticles thereof find wide applications, in pharmaceuticals, material design, such as coatings, cosmetics, optical and magnetic sensors, electronics, textiles, foods, or bio-imaging. Most intriguing are nanoparticles exhibiting a core–shell structure with deviating electrical, magnetic, optical, chemical, catalytic, or thermal properties and high biocompatibility. Particularly, polymer nanoparticles, liposomes, polymersomes, polyplexes, and carbon based nanomaterials have attracted high attention for being used as drug carrier systems to treat diseases and disease-related complications.^[2] Even more, amphiphilic polymers or block copolymers can self-assemble by means of nanoprecipitation, solvent exchange, emulsion, or dispersion polymerization, and other methods,^[3] leading to a variety of different morphologies, including latex particles with distinct surface functionalities, core–shell structures, or even inner compartments. The determination of the surface properties and the internal structure of these nanoparticles is of high interest for understanding the property(structure)-function relation of such systems.^[4] In

1. Introduction

To date, nanoparticles and nanomaterials are present in our daily life, and are involved in many technologies and industries due

Dr. C. Höppener, Prof. V. Deckert
Leibniz Institute of Photonic Technologies (IPHT) Jena
Albert-Einsteinstraße 9, 07745 Jena, Germany
E-mail: Christiane.Hoepfener@leibniz-ipht.de

Dr. C. Höppener, Prof. V. Deckert
Institute of Physical Chemistry and Abbe Center of Photonics
Friedrich-Schiller-Universität Jena
Lessingstraße 10, D-07743 Jena, Germany

 The ORCID identification number(s) for the author(s) of this article can be found under <https://doi.org/10.1002/sml.201907418>.

© 2020 The Authors. Published by WILEY-VCH Verlag GmbH & Co. KGaA, Weinheim. This is an open access article under the terms of the Creative Commons Attribution-NonCommercial License, which permits use, distribution and reproduction in any medium, provided the original work is properly cited and is not used for commercial purposes.

DOI: 10.1002/sml.201907418

Prof. F. H. Schacher
Institute of Organic Chemistry and Macromolecular Chemistry (IOMC)
Friedrich-Schiller-University Jena
Lessingstraße 8, D-07743 Jena, Germany

Prof. F. H. Schacher
Jena Center for Soft Matter (JCSM)
Friedrich-Schiller-University Jena
Philosophenweg 7, D-07743 Jena, Germany

Prof. V. Deckert
Institute of Quantum Science and Engineering
Texas A&M University
College Station, TX 77843-4242, USA

particular, core and shell (surface) region can exhibit distinct differences in terms of chemical functionality or when it comes to interactions with the surrounding medium. It is therefore important to develop tools to correlate (overall) chemical composition with local structure and functionality in such nanostructured materials. The general importance of understanding structure–function relations also manifests in the dependence of the integrity of biopolymers, proteins, and also polymer composite materials on their structure. Especially in the latter case, the chain length, packing density, or charge density have been shown to strongly influence, for example, their mechanical properties, the morphology, and the rigidity.^[5] However, due to the size, chemical diversity, and potential complexity of the used monomers and also of any structures created via self-assembly, multimodal investigations on their properties with nanoscale resolution are indispensable in order to understand their behavior in complex environments. In particular, systematically tailored design of polymeric nanostructures with distinct properties and improved functionality will benefit from the synergetic effects of multimodal and/or correlative approaches by addressing sequentially or in parallel the chemical composition, that is, the identification of functional chemical groups, nanoscale structural features, morphology changes, functionalities, and also the investigation of the mechanical properties. For this purpose, methods have attracted high attention, which enable targeting of complementary properties on the surface and internal parts of nanoparticles. Typical analytical tools utilized for the characterization of polymeric nano- and micro-particles, such as light scattering, fluorescence microscopy, and electron microscopy (EM),^[6] in general, shed only light on one of these properties, that is, they provide either chemical specificity, molecular sensitivity, dynamic or structural information. Correlative approaches aim at yielding multidimensional and corroborating information by combining various microscopy and or spectroscopic methods.^[7] As such, correlative light and electron microscopy (CLEM)^[8] and correlative light microscopy and AFM (CL-AFM)^[9] try to overcome their own limitations by pairing information on the morphology and mechanical properties with high-molecular specificity. Another still remaining challenge in terms of studying polymer nanoparticles or biological samples is their nanoscale investigation in the solvate state by means of microscopy techniques.

Raman-, infrared (IR)-spectroscopy, and mass spectrometry are unique in terms of their label-free high chemical information content, and such, satisfy the demand for correlative approaches with high chemical specificity. Whilst IR-spectroscopy and in particular secondary ion mass spectrometry (SIMS) have been already combined with super-resolution light microscopy.^[10] Recently, peak-force infrared microscopy (PFIR) has been used to simultaneously correlate chemical information with nanomechanical properties.^[11] So far, Raman spectroscopy has not been reported for usage in high-resolution correlation microscopy with super-resolution light microscopy, EM, or force–distance curve based atomic force microscopy (FD-AFM). Raman spectroscopy is widely used for bulk investigations of polymers, polymer blends, or biopolymers^[12] and can be also applied in liquid environments. However, the sensitivity of confocal Raman spectroscopy suffers by orders of magnitude from lower scattering cross sections in comparison to fluorescence and IR

investigations. In addition, the low amount of available material for individual nanoparticles demands for single molecule or single unit sensitivity, which can be accomplished by surface enhanced Raman spectroscopy (SERS) or by means of tip-enhanced Raman scattering (TERS).^[13] The latter enables to probe materials with a single-molecule sensitivity and (sub-) molecular resolution by taking advantage of the light confinement and enhancement of the electromagnetic field induced by a plasmonic tip.^[14] In this sense, TERS is a label-free technique, which combines a high chemical specificity with a high spatial resolution to obtain structural information (schematic outline, **Figure 1A**). At the same time, TERS measurements include also information on the sample topology. Recently, TERS has been also combined with tip based electrochemical measurements demonstrating the correlation of complementary information.^[15] Therefore, TERS is ideally suited to study the property–function relation of polymer nano-objects by revealing the chemical composition and structural differences based on the identification of certain marker bands and individual band positions. Several TERS studies have addressed thin films of polymer blends,^[16–18] polymerization reactions,^[19,20] and investigated structural modifications in certain biopolymers, such as fibrils.^[21] The high potential of TERS for studying weakly Raman scattering polymers under non-resonant excitation conditions has been demonstrated for ambient and also in liquid environments.^[22] As such, TERS has been shown to enable distinguishing the major components of polystyrene-polyisoprene polymer blends and to identify a heterogeneity in their distribution at the air–polymer interface and polymer–substrate interface.^[18] Similarly, TERS investigations demonstrated the identification of isotopically labeled polystyrene (PS) and common PS in miscible polymer blends.^[16] Furthermore, high-resolution tip-enhanced Raman mapping (TERM) was used to reveal phase separation in poly(methyl methacrylate)/poly(styrene-co-acrylonitrile) films.^[17] Recently, TERS was applied to study the kind and the degree of crosslinking in 2D polymers.^[20] To our knowledge, so far no TERS studies have been conducted on polymer nanoparticles or micelles. Most likely, this is due to the fact that the advanced capabilities of TERS come at the cost of a limited depth-information content, since the near-field interaction range is restricted to 2–3 nm.^[23] Hence, direct access to the interior of any nanomaterial is restricted. In order to bypass this limitation, common preparation routines for TEM investigations can be adopted to enable cross-sectional TERS investigations. Cross-sectional studies of materials rely on top-down sample preparation techniques and several methods have been exploited for this. For instance, TEM investigations of homopolymer and heteropolymer nanoparticles relied on electron beam induced radiation-damage of frozen aqueous nanoparticle dispersions, freeze-fracture techniques,^[24] or ultramicrotome slicing of resin embedded materials.^[25]

Here, we present a route toward label-free multimodal investigations of the internal structure and surface properties of polymer nanoparticles based on resin-embedded and sliced polymer nanoparticles by means of TERS, as a pivotal method, and supplementing FD-AFM spectroscopy^[26,27] (s.f. **Figure 1A**). The latter takes advantage of its ability to probe tip-sample interactions down to the piconewton range. This approach

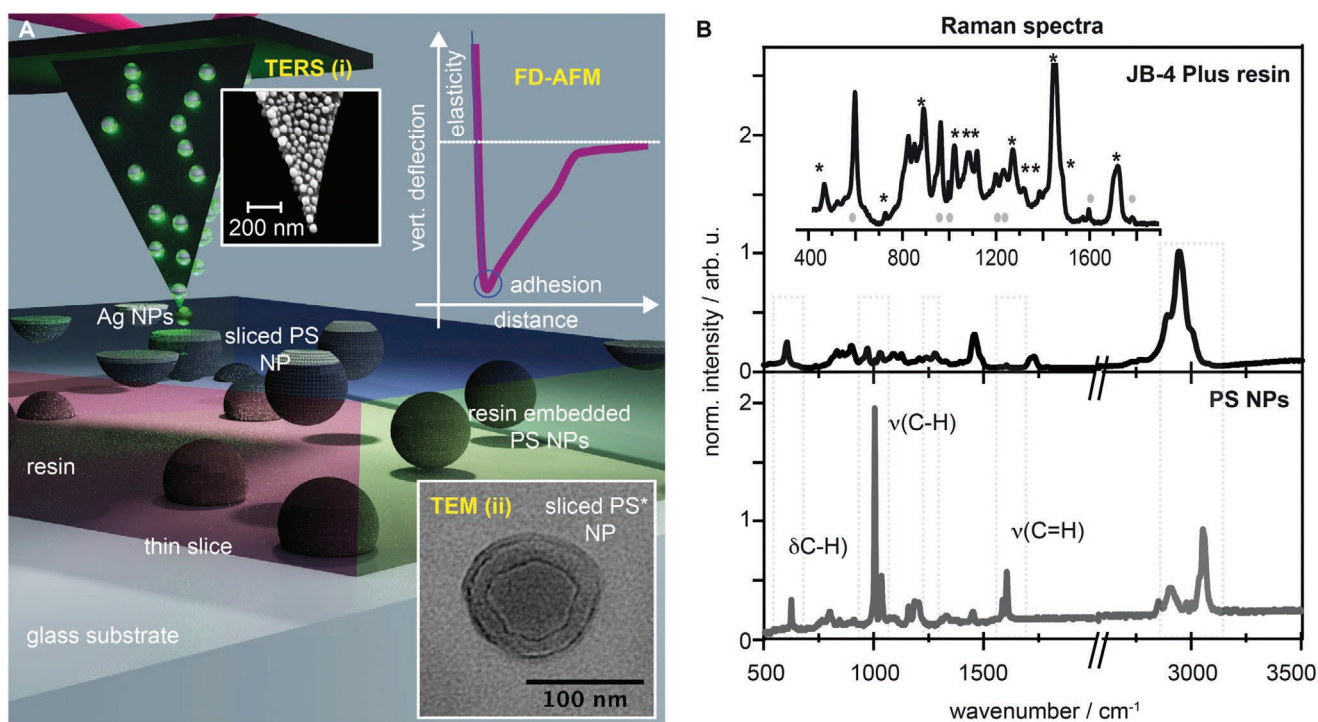


Figure 1. Multimodal investigations of polymer nanoparticles. A) Schematic outline combines TERS and FD-AFM investigations of resin embedded PS NPs. The FD-AFM measurements supplement the high chemical specificity of TERS by probing the elastic modulus and the adhesive properties of the PS NPs and the resin. Insets: SEM image of a typical TERS tip (i) and TEM image of a resin-embedded and sliced fluorescence-labeled PS nanoparticle, which reveals the core–shell structure (ii). B) Comparison of confocal Raman spectra of the used resin JB4-Plus (top) and a dense layer of PS NPs. Inset: magnification of the fingerprint region of the JB-4 Plus resin. Black asterisks label specific Raman bands of the major components of the resin, and grey dots indicate Raman bands associated to the used crosslinker.

allows to extract the elastic properties of a material, that is, the deformation, elastic moduli, energy dissipation, electrostatic repulsion, surface charge distributions, and adhesion by measuring the static force response upon nanoindentation of the tip (Figure 1A).^[28] As such, FD-AFM has been applied to investigate the nanomechanical properties of polymers,^[29–31] and biomatter.^[27,32] Combining these multiparametric studies with TERS investigations are particularly of interest for studying soft matter. Multimodal TERS-AFM investigations enable supplementing the high chemical specificity of TERS with information on the nanomechanical properties of the materials under investigations. Polystyrene nanoparticles (PS NPs) are used in the present study as a model system for demonstrating the in-depth monitoring capabilities in terms of the chemical composition, changes in the morphology, and mechanical properties. Although the TERS and FD-AFM investigations in this study are not conducted on the same sliced PS NP, an extension of this approach toward correlative studies on the same object can be established by applying the same strategies used for other advanced correlative methodologies. TEM investigations are used to prove successful slicing of the resin-embedded polymer nanoparticles, and to gain access to the internal morphology of the nanoparticle (s.f. Figure 1A(ii)). In this study, we further evaluate the ability for a spectroscopic discrimination of different polymer materials being used for nanoparticle formulation and the selected resins and also highlight that our approach can identify local structural changes in such samples. Finally,

the perspective of utilizing thin slices of materials for multimodal, correlative, or tomography investigations has fueled new interest to apply and optimize slicing procedures. For this, the resin embedding and curing steps have to be monitored, in order to identify potential preparation artifacts. We demonstrate that the presented methodology can provide detailed insights into the resin embedding and curing process, in particular, by investigating resin infiltration during the curing step.

2. Results and Discussion

2.1. Resin Embedding and Slicing of Polymer Nanoparticles

2.1.1. Selection of Resins

Appropriate resins for cellular and tissue TEM studies and for histology tissue slicing can be classified into epoxy, acryl, and paraffin formulations. In regard to the targeted TERS measurements, the used resin needs to be optically transparent, should provide low fluorescence background, and finally can be uniquely (chemically) distinguished from the polymeric compounds composing the polymer nanoparticles under investigations. Furthermore, the mechanical properties of the resin in relation to the ones of the polymer nanoparticle, differences in the hydrophilicity of the resin and the polymer nanoparticle surface, and the curing conditions have to be considered. All

selected resins are known to provide a high damage threshold upon electron beam and light exposure. In order to select suitable resins, the optical properties of acrylic resins are compared to a common epoxy resin often used for TEM investigations in terms of their fluorescence background (Figure S1, Supporting Information). Further details are provided in the Supporting Information, which include Raman spectra and corresponding band assignments for all resins (Figures S1–S3 and Tables S1–S3, Supporting Information). Based on these confocal Raman investigations, the JB-4 Plus resin is selected for further use in all TERS and FD-AFM investigations. In addition, the JB-4-Plus resin yielded the highest compatibility to reach a homogeneous distribution of the hydrophobic PS beads in the resin suspensions after resin curing.

Figure 1B (top) shows a typical confocal Raman spectrum of the selected JB-4 Plus resin along with a close-up of the fingerprint region (inset). According to the resin formulation, the Raman spectrum is governed by the C–O–C and C–C–O stretching vibrations in the spectral regions from 820 to 900 cm^{-1} and 1230–1280 cm^{-1} , which are associated to the major components, that is, 2-hydroxyethyl methacrylate (HEMA) and poly(ethylene oxide) (PEO). A complete band assignment is given in Table S1, Supporting Information. Curing of the resin occurs via radical polymerization, which induces a splitting of the C=C double bond of the acryl group. Therefore, the C=CH₂ stretching vibration at 1407 cm^{-1} and C=C aliphatic stretching vibration at 1641 cm^{-1} often are considered as a measure of the yield of polymerization of a resin.^[33] Clearly, no Raman bands appear at these positions, which demonstrates that the pure resin is well cured under the chosen polymerization conditions.

2.1.2. Discrimination of Common Polymers and the JB-4 Resins

In order to demonstrate that the selected embedding resins can be clearly differentiated from generally employed polymeric materials, Figure 1B compares the confocal Raman spectra of PS, with the confocal Raman spectrum of the JB-4-Plus resins. An extended comparison of Raman spectra taken on other polymers and other resins is given in Figure S4, Supporting Information. Particularly useful are Raman bands within the region between 1500 and 1700 cm^{-1} , which is largely silent for all resins being considered here. In particular, monomer units featuring aromatic signals such as PS

(confocal spectra, Figure 1B), or nitrogen-containing moieties such as in case of PNiPAAm and poly(*N,N*-dimethylaminoethyl methacrylate) (PDMAEMA) can be clearly distinguished from the JB-Plus resin (confocal spectra S4A). In particular, the ring deformation mode at 621 cm^{-1} , C–H stretching mode at 1002 cm^{-1} and the aromatic ring stretching modes at 1582 and 1602 cm^{-1} of the PS can be uniquely distinguished. For the PNIPAAm, the amide I band at 1656 cm^{-1} , the NH deformation band at 1621 cm^{-1} , the amide III band at 1250 cm^{-1} , and the CH₃ deformation band of the isopropyl functional group at 1401 cm^{-1} can be assigned as marker bands. This shows also the capability to distinguish peptide based polymer nanostructures. For other materials, the stretching modes of the ester carbonyl groups occurring in the 1650–1750 cm^{-1} region (C=O stretching) and in the 800–900 cm^{-1} region (the COO stretching) can also be considered for distinguishing between polymer and resin (comparison of polymers and resins, Figure S4, Supporting Information).

2.1.3. TEM Characterization of Sliced PS NPs

Taking the mentioned marker bands of various polymers into account, it can be expected that polymer nanoparticles formulated from a broad variety of polymers can be distinguished with high fidelity from the targeted acryl resins by means of TERS (Figure 1B). Here, we focus on PS NPs, since these are largely mono-disperse and commercially available. Furthermore, the PS NPs are an extensively used platform for studying the formation of a protein corona and stealth properties of polymers. Both issues can be ideally approached by the presented methodology in the future. Therefore, both unmodified hydrophobic PS beads and hydrophilic fluorescent PS beads (from now on denoted as PS* NPs) with a nominal diameter of 100–120 nm (± 15 nm for the PS NPs and ± 20 nm for the PS* NPs) as specified by the manufacturer are used here as model system in order to investigate the embedding procedure. The hydrophilic PS* NPs mix well with all resins. To demonstrate that the ultramicrotome slicing of resin embedded nanoparticles also leads to the sectioning of the nanoparticles, PS* beads are embedded in the Lowicryl resin (LWC) and the cured block is sliced with a diamond knife. Here, slices with a thickness down to ≈ 50 nm can be obtained and are investigated by TEM (Figure 2). According to the nominal diameter of ≈ 100 nm, the observed nanoparticle size in the TEM

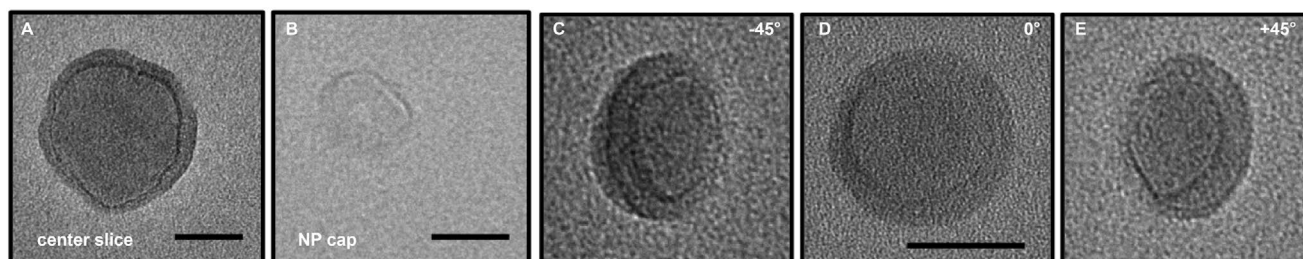


Figure 2. TEM investigations of thin slices of fluorescent PS beads with a nominal diameter of 100 nm embedded in the JB-4 Plus resin. A,B) TEM images of typically found structures representing PS NPs being sliced at different heights, that is, a center sliced NP and nanoparticle caps. Selected TEM images of a tilt series acquired at tilt angles of C,E) $\pm 45^\circ$ C and D) 0° . A movie of the entire tilt series is provided in Movie S4, Supporting Information. Scale bars: 50 nm

images is apparently smaller. Therefore, the observed structures can be identified as nanoparticle caps (s.f. Figure 2B) or nanoparticles which have been sliced not at the center (s.f. Figure 2A). From the TEM images, it seems that the core of the PS* NP is surrounded by a shell-like structure. Thus, the observed structure can be assigned to the incorporated fluorescent dye molecules and most likely to the surface functionalization. In order to verify that the PS* NPs are indeed sliced, and thus, the interior of the nanoparticle can be accessed, a tilt series of individual NPs is acquired (full tilt series is provided in Movie S1, Supporting Information). Figures 2C,E show the corresponding TEM images of the $\pm 45^\circ$ tilt positions next to the center position (0° tilt, Figure 2D). The change in the geometry upon tilting the sample stage clearly shows that the nanoparticle does not anymore exhibit a spherical shape, but rather takes on the geometry of a half-sphere.

Since the PS* NPs are not suitable for the finally targeted Raman spectroscopy investigations, also unmodified PS beads have been embedded in all resins. It turns out that the JB-4-Plus resin yields the most homogenous samples of randomly distributed, isolated PS beads. However, due to the targeted high density of nanoparticles and the long curing times at cold temperatures, a partial aggregation of the PS beads could not be prevented (s.f. Figure S5, Supporting Information).

2.2. TERS Investigations of Resin-Embedded and Sliced PS NPs

So far, the TEM investigations demonstrate that the embedded polymer nanoparticles can be sectioned, and thus, access to the interior of the nanoparticles is provided. However, the TEM investigations provide no information on the embedding process itself. Incubation and incorporation of the polymer nanoparticles within the resin might lead to an infiltration of the PS NP, leading to altered chemical and mechanical properties of the nanoparticles after the curing process. TERS maps with high chemical specificity and high spatial resolution may provide additional insights into the embedding process.

At first, the TERS investigations have to demonstrate that polymer and resin can be uniquely discriminated on the nanoscale. Therefore, the thin sections of PS NPs are studied by means of TERS either by acquiring a set of spectra along a predefined line or predefined grid positions. The acquisition time for each spectrum is typically 1 s using an excitation power of $650 \mu\text{W}$. Figure 3A shows a topography image of a sliced nanoparticle next to a sequence of TERS spectra. The marked positions in the AFM image correspond to the positions where sequential TERS spectra have been acquired across the PS NP-resin interface with a spatial separation between the adjacent spectra positions of $\approx 10 \text{ nm}$. For comparison, a TERS spectrum acquired on a spin-casted PS film is shown at the top of Figure 3A. Taking into account the above assigned marker bands for the PS, the TERS spectra 1–4 clearly show the ring bending/stretching combination band at 1604 cm^{-1} . The 1002 cm^{-1} RBM peak is not clearly visible in the TERS spectra due to an overlap with the overtone mode of the Si-peak (520 cm^{-1}) of the TERS-tip. Furthermore, the high in-plane/out-of-plane orientation sensitivity of this mode in TERS due to the longitudinal polarization of the exciting electromagnetic field of the TERS tip might strongly reduce the presence of this Raman band in TERS.

At position 5, the TERS spectrum changes. In particular, the intensity of the CH ring bending/stretching mode at 1602 cm^{-1} strongly decreases and instead a band at $\approx 1630 \text{ cm}^{-1}$ appears. The latter likely corresponds to the C=C aliphatic stretching vibration of the resin precursor. This indicates that the curing process of the resin is less efficient for a mixture of resin and PS NP suspensions compared to the plain resin. Since also Raman signatures assignable to internal modes of the PS disappear (CH stretching modes at 1070 , 1250 , 1430 , and 1520 cm^{-1}), the PS NP can be clearly spatially distinguished from the resin. The transition from the PS to the resin at position 5 coincides well with the localization of the PS NP found in the acquired topography image.

TERS mapping across the entire sliced surface of the PS NP and the surrounding resin has been carried out to further investigate the homogeneity and the crystalline state of the PS. Furthermore, the homogeneity of the resin in terms of the curing degree

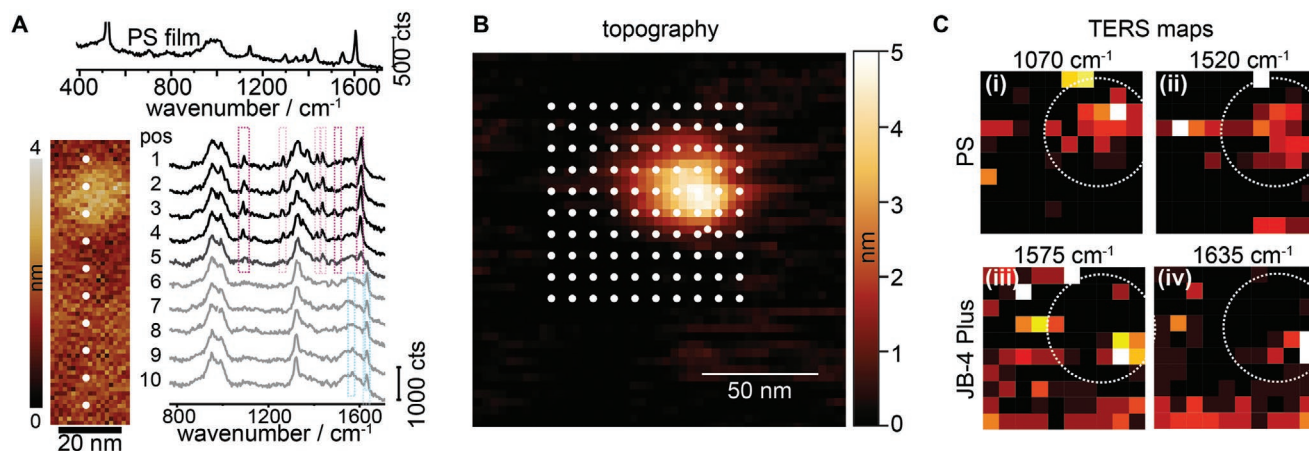


Figure 3. TERS of resin embedded and sliced NPs. A) TERS spectra of a resin embedded and sliced PS NP acquired across the interfacial PS NP resin area as indicated by the dashed line in the corresponding topography scan (left). Top: TERS spectrum of a spin-coated PS film for reference. B) AFM topography image of a resin embedded and sliced PS NP displayed together with the utilized grid for the TERS mapping shown in (C). C) Intensity maps of selected marker bands for i,ii) PS and iii,iv) the resin (correspond to the sliced PS NP identified in the topography image (B)).

is approached by this mapping in more detail. Figure 3B provides an example of a sliced PS NP. The topography image shows the sliced PS NP with the superimposed TERS grid used for the TERS mapping in Figure 3C. The grid is composed of 10×10 spectra leading to a distance of adjacent spectra positions of ≈ 10 nm. Selected marker bands of PS and the resin have been transferred into intensity plots by summation of the spectral band intensities (s.f. Figure 3C). The top row of images shows the distribution of selected PS-specific marker bands (1070 and 1520 cm^{-1}) as assigned in Figure 3A. Clearly, these bands appear in the expected region where the sliced NP has been identified according to the topography image shown in Figure 3B. In contrast, images referring to the selected resin marker bands show different distributions. In particular, the resin bands at 1575 and 1635 cm^{-1} band almost disappear in the PS NP region as expected. However, a closer inspection of the distributions of the resin marker bands reveals a region associated to the sliced PS NP, where resin marker bands appear (bottom right area). This might be an indication of a minor infiltration effect of the resin in the interfacial region of the PS NP during the curing process. However, if so, the infiltration of resin compounds seems to occur only locally and only at the interface between NP and resin.

2.3. FD Based AFM Investigations of the Nanomechanical Properties

A potential infiltration of resin compounds should also impart the nanomechanical properties of the PS NPs locally. Therefore, slices of JB-4-Plus embedded PS NPs are investigated by means of FD-AFM to obtain adhesion and elasticity maps of individually sliced PS NPs. As schematically outlined in Figure 1A, force–distance curves are acquired to deduce the elasticity properties by means of a nanoindentation of the tip. The indentation depth is limited by setting the force setpoint to 0.5 – 1 nN. Clear differences in the mechanical properties are found for the resin itself and the PS NP.

Figure 4A provides an overview of the randomly distributed resin-embedded and sliced PS NPs. The PS NPs can be clearly identified in the topography due to their slight protrusion from the resin surface (s.f. Figure 4A(iii)). The height of these protrusions varies from 1 nm for the smaller structures to ≈ 15 nm for NPs with the largest diameter. It can be expected that due to a slight compression of the beads during the curing process, the softer PS oozes gently out at the sliced interface. However, the sliced NPs maintain largely a spherical shape, which indicates that the modification of the stiffness of the surrounding resin during the curing process does not lead to larger deformations of the PS NPs. Taking into account the spherical geometry, the diameter of the projected area of the sliced nanoparticles is expected to be smaller than the diameter of the intact PS beads. The simultaneously recorded maps of the mechanical properties of the PS beads and the resin are shown in Figure 4A(i),(ii). Corresponding averaged FD curves for the extension and the retraction of the tip are shown in Figure 4B(i),(ii). Furthermore, typical individual FD curves are shown in Figure S6, Supporting Information to provide an estimate for the homogeneity. Clearly the FD curves reveal differences in the elastic modulus and the adhesion for the PS and the resin. These changes of the mechanical properties are

confined to the projected area of the NPs. The adhesion contrast between the resin and the NP can be related to the use of a hydrophilic resin, whilst the PS nanoparticles are hydrophobic. The response of the AFM tip upon the interaction with both materials is controlled by the polarity of the SiO_2 layer of the AFM tip. As such, a lower adhesion force is measured on the hydrophobic PS NPs compared to the hydrophilic resin (FD curve, Figure 4B(ii)). In addition, the elasticity measurements demonstrate the expected differences in the stiffness for the present materials. Considering the cantilever properties, the elasticity maps can be transferred into the elasticity modulus (M_E) providing a measure for the stiffness of the different materials. Clearly the cured resin exhibits a higher stiffness ($\approx 2\times$) compared to the embedded PS NPs (Lineprofile, Figure 4C(i)). In addition, Figure 4C(ii) displays the distribution of found M_E values averaged across the NP interface. The mean M_E is determined to be 4.6 GPa, which is in good agreement with the known value of solid PS of 3.5 GPa and PS regions of 2 – 3 GPa.^[31,34] The slight deviations most likely arise from the unknown real tip shape/size, may be related to the preparation of the PS NP itself, or potential influences from the resin environment, for example, slight swelling.^[35] NP size and potential bottom deformation, which have been identified as possible influences affecting the measured elastic modulus can be excluded in these experiments.^[30]

However, taking a closer look at the homogeneity of the elastic modulus across different sliced PS NPs, deviations for NPs with similar projected area are found (s.f., e.g., arrows in Figure 4A(i)). In order to exclude any influence of the degree of curing in the direct vicinity, the relative elastic modulus ΔM_E , as defined in Section 4 (s.f. Equation (1)), is determined from the apparent M_E values and plotted as function of the projected NPs surface area (s.f. Figure 4D). Clearly, a large variation of the ΔM_E values for structures with a small and large projected area is found, respectively. The increase of the ΔM_E with increasing projected area approaches a constant ΔM_E value of 3.5 GP (± 1 GPa). For nanoparticles sliced in the region of the nanoparticle caps, that is, structures with a small projected area, the ΔM_E obeys a higher variance than for center-sliced NPs. In addition, a steep increase in ΔM_E is observed. A model is suggested as outlined in Figure 4E, which can explain these experimental observations. Both the steep increase as well as the higher fluctuations can be assigned to different sub-surface material properties, since the elasticity measurements partly reflect the stiffness of the underlying materials (so-called bottom-effect).^[35] The slicing of the PS nanoparticles in the top, center, and bottom part of a PS bead leads to different sub-surface configurations. A top to center slicing of the NPs results in sliced NPs, which are largely supported by a block of softer PS, and thus, leads to a larger distance to the resin substrate. In contrast, for bottom sliced NPs, the distance to the resin substrate is reduced, and consequently, the influence on the stiffer resin support increases. Besides revealing the nanomechanical properties of the investigated NPs and the resin, due to the bottom effect artifact,^[36,37] the FD-AFM investigations are capable to determine the slicing point, that is, if an NP is sliced in its top or bottom half, due to its extraordinary sensitivity. The latter cannot be accessed by common AFM imaging, since top and bottom sliced result in the same diameter of the projected area. In principle, the data

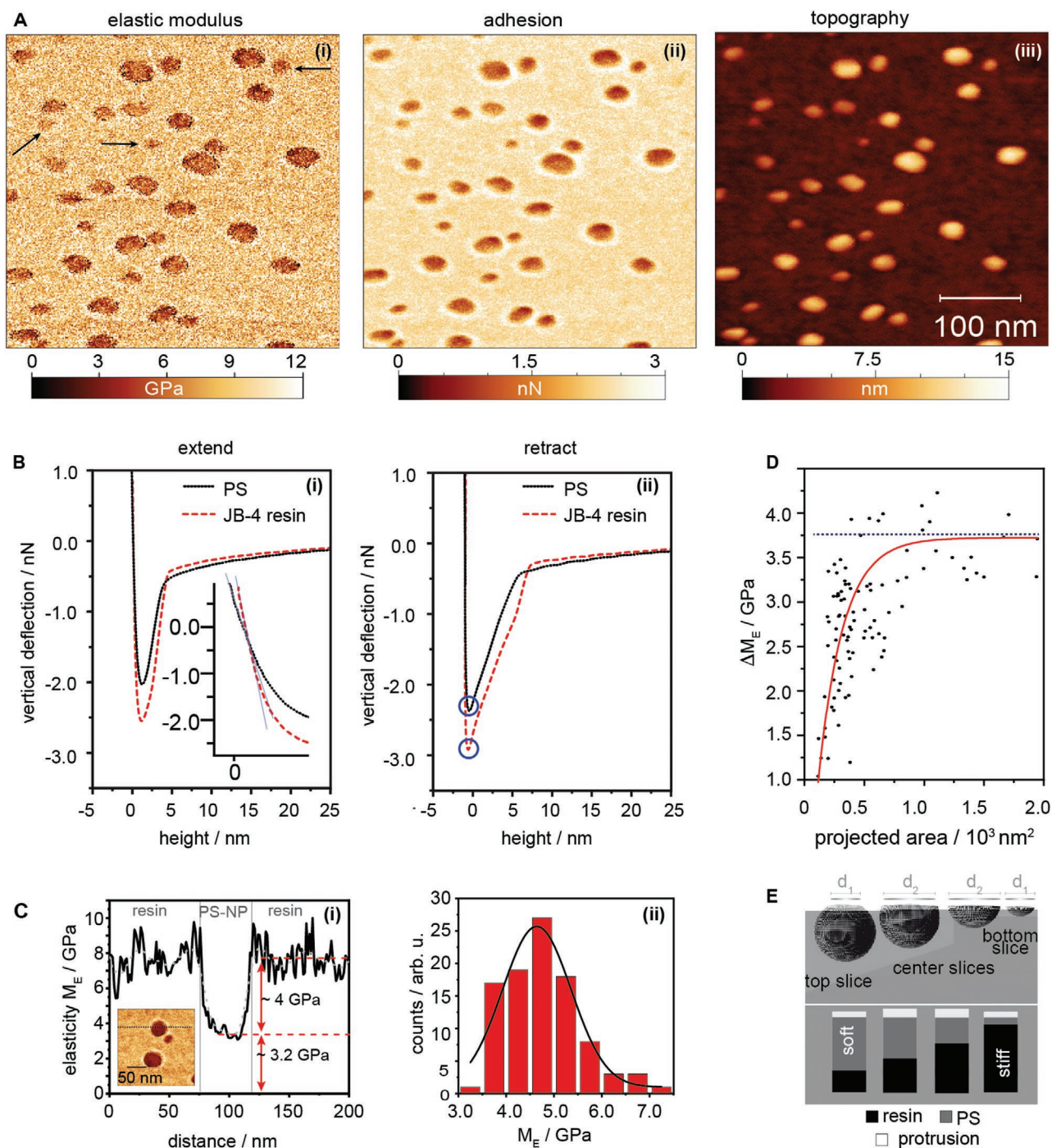


Figure 4. Nanomechanical properties of randomly distributed, resin embedded, and sliced PS nanoparticles determined by means of FD based AFM spectroscopy. A) Simultaneously acquired elasticity (i), adhesion (ii), and topography (iii) images revealing the different nanomechanical properties of the resin and the PS NPs. The elasticity data represent apparent modulus values. B) Average of 128 typically recorded extension (i) and retract (ii) FD curves recorded on the resin and the PS NPs. C) Cross section of the elastic modulus across an individual PS NP as shown in the inset (i) and distribution of the averaged M_E across the sliced area of a large number of PS nanoparticles. D) Changes in the mean relative elastic modulus ΔM_E of individual PS nanoparticles as a function of the projected area of the sliced interface. E) Scheme of the expected substrate influence on the elasticity measurements.

could be corrected for this bottom effect artifact^[37,38]; however, the possibility of determining the slicing plane, is of interest in regard to investigations of polymer systems with more complex morphologies.

2.4. Influence of the Resin Embedding on the PS NP Properties

In order to further investigate the hypothesis of resin infiltration during the embedding process, individually sliced PS NPs are

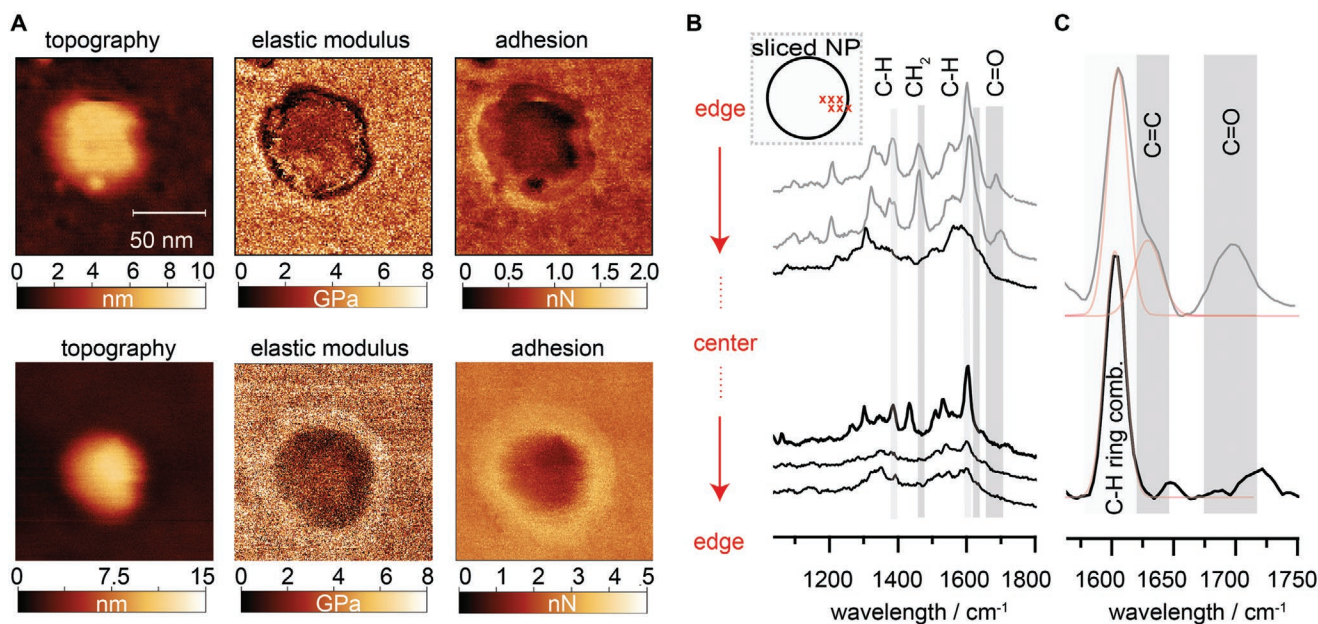


Figure 5. Independent FD-AFM and TERS investigations of a potential infiltration of resin components. A) High-magnification topography, elastic modulus, and adhesion maps of individual resin-embedded and sliced PS NPs show varying nanomechanical properties in the interfacial region. The elasticity data represent apparent modulus values. B) Selected spectra of an interfacial PS NP resin region (as schematically indicated in the inset) showing a mixture of PS and resin at the interface and pure PS spectra toward the center of the NPs. C) Zoom-in to the spectral region from 1550 to 1750 cm^{-1} , which shows a clear asymmetry for the 1604 cm^{-1} band (CH ring combination band) and the carbonyl stretching mode at 1700 cm^{-1} for the top spectra, which are acquired directly at the resin PS NP interface. In contrast the C=O stretching mode and the asymmetry of the CH ring bending/stretching combination band disappear for the bottom spectra. The presence of the CH ring combination band, the C=C stretching mode, and the C=O stretching mode is indicative for a localized infiltration of the resin.

investigated for a change in their mechanical properties across the sliced surface, and in particular, in the interfacial region. Therefore, elasticity and adhesion maps with high resolution are generated for individual sliced PS NPs. **Figure 5A** displays the simultaneously probed topography, elastic modulus, and adhesion maps of sliced PS NPs. Whilst the PS NP displayed in the bottom row shows relative homogeneous mechanical properties across the sliced NP surface, the top example shows some locally confined inhomogeneity, which could also point to an infiltration of the NP with resin. In principle, a change in the elasticity can be also of non-chemical origin, but induced by amorphous and crystalline phases. Taking into account the TERS investigations, the band positions of the PS marker bands correspond to the known position for amorphous PS, and thus, the TERS measurements proved the expected amorphous state of the PS in the NPs. As a consequence, the measured minor changes in the stiffness across the interior of the PS NP beads cannot be ascribed to crystallization occurring in our opinion. In addition, alterations in the hydrophilicity of the resin are observed in the adhesion measurements. In particular, a higher adhesion is found at the interfacial boundary between the resin and the PS NP. This higher hydrophilicity might be caused by H_2O inclusions due to the formation of a hydration layer during the curing process. This hydration layer might lead to a lower conversion during the polymerization process. The TERS investigations support this assumption, for example, in **Figure 3A**, the C=C aliphatic stretching mode appears still at a distance of $\approx 25\text{--}50$ nm. However, the M_E map does not indicate the expected lower stiffness in the interfacial

region of the resin, which seems at first in contradiction to the assumption of hydration effects. Here, it has to be considered, that the elasticity measurements and the Hertz model to extract the M_E assume that other material properties remain constant. Therefore, higher adhesion in this region might mislead to an apparent higher elasticity, due to changed wetting conditions of the tip. The impact of the wetting and adhesion has been addressed in a recent study, which explains the observed discrepancies for bulk and nanoscale determination of the elastic sample properties for crosslinked polydimethylsiloxane to arise by an increase of the contact area, and thus, a decrease of the applied stress.^[39] Since the indentation depths used in these investigations is much larger (550–1000 nm) than the ones used here, these cannot be directly transferred to the situation shown in **Figure 5A**. However, the study demonstrates that changes in the sample homogeneity may induce incorrect local elasticity moduli. This is also supported by the example shown at the top of **Figure 5A**, where the adhesion does not change as much as for the top example, and thus, does not strongly impart the elasticity measurements. Theoretically, it has been shown, that a reliable measurement of the nanomechanical properties requires data acquisition rates for which the inertial and hydrodynamic contributions to the measured forces–distance curve can be neglected.^[27] Typically, this can be achieved for a ratio of the fundamental cantilever resonance and the modulation frequency in the range of 50 for the elasticity modulus and >300 for the adhesion, which complies with the chosen data acquisition rates in **Figures 4** and **5A**. Taking a closer look at the details of the TER spectra acquired in the

interfacial region of a sliced PS NP, clearly varying characteristic peaks are found (s.f. Figure 5B). The two spectra being closest to the PS-resin interface (top spectra) show clearly marker bands of both PS and the resin. Besides the asymmetry of the CH ring bending/stretching mode of PS, the carbonyl vibration is clearly visible (TER spectra, Figure 5C). The asymmetry of the CH combination band at 1600 cm^{-1} stems from occurring C=C aliphatic stretching mode at 1630 cm^{-1} . In contrast, other spectra acquired toward the center of a PS NP but still located close to the interfacial region show purely PS marker bands and no asymmetry of the CH combination band (s.f. Figure 5B,C). These TER spectra clearly demonstrate that resin infiltration preferentially occurs in the interfacial region and only occurs locally. Therefore, the TERS investigations are in excellent agreement with independent observation of the nanomechanical investigations, both in terms of a minor localized infiltration, and also in regard to the observed altered degree of polymerization of the resin.

3. Conclusion

We herein demonstrate that a combination of multimodal TERS and FD-AFM investigations can be used to access chemical functionality, nanoscale structure, and internal morphology of PS NPs. Whereas TERS provides information about chemical functionality at nanoscale resolution, complementary FD-AFM spectroscopy allows to extract information about stiffness and (local) hydrophilicity. For this, we established embedding and slicing protocols using various resins and also performed control experiments with different materials. As TEM can also be used to access, for example, the morphology structure of such nanostructures, we foresee great potential for correlative TERS/TEM investigations. We could also show that infiltration of the resin into the PS NP is almost neglectable. The presented TERS and complementary adhesion and elasticity measurements revealed no impact of the resin embedding and slicing process on the nanomechanical properties and geometry of the PS NPs. Hence, this study confirms that the resin embedding process is a suitable approach for future studies addressing the local morphology of, for example, more complex drug carrier systems by means of TERS.

The potential of this multimodal approach utilizing TERS as a key methodology opens up new perspectives in terms of understanding the property-function relation of polymeric nanostructures in general. The unique possibilities of TERS enable to study the homogeneity, local functionality, crystallinity, and any interfacial transition regions occurring. With that, this approach outperforms and complements other techniques for NP characterization, which are frequently limited only to individual aspects of structure–function relations, and provides the perspective to utilize the obtained information to iteratively improve structure–function properties.

4. Experimental Section

Materials: Commercially available resins were used in this study. The JB-4-Plus resin kit was purchased from Polysciences Europe GmbH, Germany. 2.5 mL of the monomer solution were mixed with the 31 mg

catalyst until it is completely dissolved. Sequentially, 100 μL of the accelerator solution was added. Curing was carried out at $4\text{ }^\circ\text{C}$ for 24 h in a Beem capsule. Lowicryl KM4 resin was highly cross-linked, polar, and hydrophilic. Monomer, crosslinker, and initiator were purchased from Polysciences GmbH, Germany. 1.73 g of the monomer and 270 mg of the crosslinker were mixed using a nitrogen stream to avoid the incorporation of oxygen in the resin. After thorough mixing, 10 mg of the photoinitiator benzoin ethylether were added and continuously mixed until the initiator was completely dissolved. UV light ($\lambda_{\text{exc}} = 265\text{ nm}$, $P_{\text{exc}} = 36\text{ W}$) curing was carried out at $4\text{ }^\circ\text{C}$. The detailed composition of all resins is provided in the Supporting Information.

PS beads (LB1) with a typical diameter of 100 nm were purchased from Sigma Aldrich Inc., Germany. Prior to use, the aqueous suspensions were purified by centrifugation of 500 μL solution at 15 000 rpm for 30 min. The supernatant solution was aspirated and the remaining pellet containing the PS beads was re-suspended in Milli-Q water ($18\text{ M}\Omega\text{ cm}$) to a volume of 500 μL . The centrifugation and suspension steps were repeated three times. PS* NPs (L9904) loaded with an orange fluorescent dye were purchased from Sigma Aldrich Inc., Germany. The stock solution was used without any purification steps.

For embedding of the PS NPs, freshly prepared resin solutions were used. 50 μL of each bead solution were mixed with 800 μL of the resin solution by means of gentle agitation. Curing of the sample followed the procedures described above.

The cured resin blocks were removed from the Beem capsules and sliced with an ultramicrotome (RMC PowerTome PTXL, Boeckerler Instruments Inc., USA). The trimmed block was sliced either with a glass knife or a diamond knife (Diatome Ltd., Switzerland). Depending on the knife used, the thickness of the obtained sliced was 300–50 nm. The slices were either adhered to carbon coated Cu grids for TEM (Plano GmbH, Germany) investigations or glass coverslips for scanning probe microscopy (SPM) and TERS investigations by means of water bonding. All glass substrates were cleaned in a Piranha solution (mixture of nitric acid and hydrogen peroxide with a ratio of 3:1) for 3 h. Afterward, the cleaned coverslips were rinsed with deionized water and dried with nitrogen.

Methods: TEM investigations used a G²20 Technai (FEI Technologies, USA). An acceleration voltage of 200 kV was typically used. Tilt series were acquired choosing tilting steps of 1° .

TERS investigations were carried out with a JPK system, which combined an AFM platform with a Raman spectrometer. The system comprised an inverted microscope (Olympus, Germany) using a 60 \times oil immersion objective with NA of 1.45. Samples were excited by means of a linearly polarized laser beam with an excitation wavelength of 532 nm and an excitation power of 650 μW , which was tightly focused on the sample by the objective. The Raman signal was collected by the same objective, and sent to a Raman spectrometer composed of a spectrograph (Acton Advanced SP 2750A, Princeton Instruments, USA) and a coupled Peltier-cooled CCD camera (Pixis 256, Princeton Instruments, USA). The acquisition time of the TERS spectra was 1 s. TERS tips were prepared by coating commercially available Si cantilever tips (Tap-190-Al, Budget Sensors, Germany) with a 2 nm silver film by means of thermal evaporation. Sequential annealing of the Ag-coated tips led to the formation of $\approx 40\text{ nm}$ Ag nanoparticles decorating the Si tip. The TERS tips were stored in an inert argon atmosphere until usage.

AFM topography and QI-mode adhesion and elasticity measurements utilized the Nanowizard 3 SPM system (JPK Instruments AG, Germany). For routine AFM topography measurements, the Tap-190-Al cantilevers (Budget Sensors, Germany) with a resonance frequency of 190 kHz and a spring constant of 35 N m^{-1} were used. For the advanced QI mode adhesion and elasticity measurements, softer cantilevers with a resonance frequency of 150 kHz and a spring constant of $4\text{--}5\text{ N m}^{-1}$ (Conti-150-Al, Budget sensor, Germany) were used. Force–distance curves were recorded with a modulation frequency of 200–250 Hz. Therefore, the resultant ratio of the resonance frequency and the modulation frequency yielded 600–750. The relative elastic modulus was determined from the experimental data, after fitting the FD curves with a Hertz model using a Poisson ratio of 0.35. All elastic modulus

values corresponded to the apparent values and had not been corrected for the bottom effect artifact. Therefore, the measured elastic modulus M_E^{PS} was averaged across the entire projected area of the sliced PS NP. The average elastic modulus M_E was determined across a similar area surrounding the PS NP.

The relative elastic modulus was then given by the difference of both quantities

$$\Delta M_E = \left| \overline{M_E} - \overline{M_E^{PS}} \right| \quad (1)$$

Supporting Information

Supporting Information is available from the Wiley Online Library or from the author.

Acknowledgements

The authors acknowledge funding from the Deutsche Forschungsgemeinschaft (DFG, German Research Foundation)—project number 316213987—SFB 1278 PolyTarget (projects B04, C04, and Z01). The authors thank S. Hoepfner (Jena Center for Soft Matter (JCSM)) for conducting the TEM investigations and D. Friedrich for fruitful discussions on the resin embedding and slicing procedures.

Conflict of Interest

The authors declare no conflict of interest.

Keywords

force–distance curve based atomic force microscopy, microtome slicing, multimodal characterization, polymer nanoparticles, resin embedding, tip-enhanced Raman spectroscopy

Received: December 18, 2019

Revised: January 27, 2020

Published online: March 29, 2020

- [1] R. Ghosh Chaudhuri, S. Paria, *Chem. Rev.* **2012**, *112*, 2373.
- [2] a) M. Karimi, A. Ghasemi, P. Sahandi Zangabad, R. Rahighi, S. M. Moosavi Basri, H. Mirshekari, M. Amiri, Z. Shafaei Pishabad, A. Aslani, M. Bozorgomid, D. Ghosh, A. Beyzavi, A. Vaseghi, A. R. Aref, L. Haghani, S. Bahrami, M. R. Hamblin, *Chem. Soc. Rev.* **2016**, *45*, 1457; b) A. Kumari, S. K. Yadav, S. C. Yadav, *Colloids Surf., B* **2010**, *75*, 1; c) O. C. Farokhzad, R. Langer, *ACS Nano* **2009**, *3*, 16; d) D. A. Christian, S. Cai, D. M. Bowen, Y. Kim, J. D. Pajeroski, D. E. Discher, *Eur. J. Pharm. Biopharm.* **2009**, *71*, 463; e) K. Kataoka, A. Harada, Y. Nagasaki, *Adv. Drug Delivery Rev.* **2012**, *64*, 37.
- [3] a) J. Pecher, S. Mecking, *Chem. Rev.* **2010**, *110*, 6260; b) B. Charleux, G. Delaittre, J. Rieger, F. D'Agosto, *Macromolecules* **2012**, *45*, 6753; c) U. Bilati, E. Allémann, E. Doelker, *Eur. J. Pharm. Sci.* **2005**, *24*, 67; d) F. H. Schacher, P. A. Rupar, I. Manners, *Angew. Chem., Int. Ed.* **2012**, *51*, 7898; e) A. H. Gröschel, F. H. Schacher, H. Schmalz, O. V. Borisov, E. B. Zhulina, A. Walther, A. H. E. Müller, *Nat. Commun.* **2012**, *3*, 710.
- [4] a) A. Verma, O. Uzun, Y. Hu, Y. Hu, H.-S. Han, N. Watson, S. Chen, D. J. Irvine, F. Stellacci, *Nat. Mater.* **2008**, *7*, 588; b) R. C. Van Lehn, P. U. Atukorale, R. P. Carney, Y.-S. Yang, F. Stellacci, D. J. Irvine, A. Alexander-Katz, *Nano Lett.* **2013**, *13*, 4060; c) H.-M. Ding, Y.-Q. Ma, *Small* **2015**, *11*, 1055; d) S. L. Tao, T. A. Desai, *J. Controlled Release* **2005**, *109*, 127; e) S. Wang, H. Guo, Y. Li, X. Li, *Nanoscale* **2019**, *11*, 4025; f) C. E. de Castro, C. A. S. Ribeiro, A. C. Alavarse, L. J. C. Albuquerque, M. C. C. da Silva, E. Jäger, F. Surman, V. Schmidt, C. Giacomelli, F. C. Giacomelli, *Langmuir* **2018**, *34*, 2180.
- [5] S. Cheng, B. Carroll, W. Lu, F. Fan, J.-M. Y. Carrillo, H. Martin, A. P. Holt, N.-G. Kang, V. Bocharova, J. W. Mays, B. G. Sumpter, M. Dadmun, A. P. Sokolov, *Macromolecules* **2017**, *50*, 2397.
- [6] a) N. Rajabalinia, S. Hamzehlou, E. Modin, A. Chuvilin, J. R. Leiza, J. M. Asua, *Macromolecules* **2019**, *52*, 5298; b) M. M. Modena, B. Rühle, T. P. Burg, S. Wuttke, *Adv. Mater.* **2019**, *31*, 1901556.
- [7] a) M. A. G. Gosecka, M. Colloid, *Polym. Sci.* **2015**, *293*, 2719; b) M. Hauser, M. Wojcik, D. Kim, M. Mahmoudi, W. Li, K. Xu, *Chem. Rev.* **2017**, *117*, 7428; c) P. S. Popp, J. F. Herrmann, E.-C. Fritz, B. J. Ravoo, C. Höppener, *Small* **2016**, *12*, 1667.
- [8] a) E. Brama, C. J. Peddie, M. L. Jones, M.-C. Domart, X. Snetkov, M. Way, B. Larijani, L. M. Collinson, *J. Chem. Biol.* **2015**, *8*, 179; b) P. de Boer, J. P. Hoogenboom, B. N. Giepmans, *Nat. Methods* **2015**, *12*, 503; c) C. van Rijnsoever, V. Oorschot, J. Klumperman, *Nat. Methods* **2008**, *5*, 973.
- [9] a) W. C. Duim, B. Chen, J. Frydman, W. E. Moerner, *ChemPhysChem* **2011**, *12*, 2387; b) P. D. Odermatt, A. Shivanandan, H. Deschout, R. Jankele, A. P. Nievergelt, L. Feletti, M. W. Davidson, A. Radenovic, G. E. Fantner, *Nano Lett.* **2015**, *15*, 4896.
- [10] a) S. K. Saka, A. Vogts, K. Kröhnert, F. Hillion, S. O. Rizzoli, J. T. Wessels, *Nat. Commun.* **2014**, *5*, 3664; b) D. R. Whelan, T. D. M. Bell, *ACS Chem. Biol.* **2015**, *10*, 2874.
- [11] H. Wang, L. Wang, D. S. Jakob, X. G. Xu, *Nat. Commun.* **2018**, *9*, 2005.
- [12] J. L. Koenig, *Spectroscopy of Polymers*, 2nd ed., Elsevier Science Inc., New York **1999**.
- [13] a) M. D. Sonntag, J. M. Klingsporn, A. B. Zrimsek, B. Sharma, L. K. Ruvuna, R. P. Van Duyne, *Chem. Soc. Rev.* **2014**, *43*, 1230; b) T. Deckert-Gaudig, A. Taguchi, S. Kawata, V. Deckert, *Chem. Soc. Rev.* **2017**, *46*, 4077.
- [14] a) X. Chen, P. Liu, Z. Hu, L. Jensen, *Nat. Commun.* **2019**, *10*, 2567; b) S. Jiang, X. Zhang, Y. Zhang, C. Hu, R. Zhang, Y. Zhang, Y. Liao, Z. J. Smith, Z. Dong, J. G. Hou, *Light: Sci. Appl.* **2017**, *6*, e17098; c) R. Zhang, Y. Zhang, Z. C. Dong, S. Jiang, C. Zhang, L. G. Chen, L. Zhang, Y. Liao, J. Aizpurua, Y. Luo, J. L. Yang, J. G. Hou, *Nature* **2013**, *498*, 82.
- [15] G. Kang, M. Yang, M. S. Mattei, G. C. Schatz, R. P. Van Duyne, *Nano Lett.* **2019**, *19*, 2106.
- [16] R. L. Agapov, J. D. Scherger, A. P. Sokolov, M. D. Foster, *J. Raman Spectrosc.* **2015**, *46*, 447.
- [17] L. Xue, W. Li, G. G. Hoffmann, J. G. P. Goossens, J. Loos, G. de With, *Macromolecules* **2011**, *44*, 2852.
- [18] B.-S. Yeo, E. Amstad, T. Schmid, J. Stadler, R. Zenobi, *Small* **2009**, *5*, 952.
- [19] Z. Zhang, M. Richard-Lacroix, V. Deckert, *Faraday Discuss.* **2017**, *205*, 213.
- [20] V. Müller, F. Shao, M. Baljovic, M. Moradi, Y. Zhang, T. Jung, W. B. Thompson, B. T. King, R. Zenobi, A. D. Schlüter, *Angew. Chem., Int. Ed.* **2017**, *56*, 15262.
- [21] a) T. Deckert-Gaudig, V. Deckert, *Sci. Rep.* **2016**, *6*, 39622; b) D. Kurouski, T. Deckert-Gaudig, V. Deckert, I. K. Lednev, *J. Am. Chem. Soc.* **2012**, *134*, 13323; c) M. Paulite, C. Blum, T. Schmid, L. Opilik, K. Eyer, G. C. Walker, R. Zenobi, *ACS Nano* **2013**, *7*, 911.
- [22] N. Kumar, W. Su, M. Vesely, B. M. Weckhuysen, A. J. Pollard, A. J. Wain, *Nanoscale* **2018**, *10*, 1815.
- [23] a) S. Trautmann, J. Aizpurua, I. Götz, A. Undisz, J. Dellith, H. Schneidewind, M. Rettenmayr, V. Deckert, *Nanoscale* **2017**, *9*, 391; b) T. Deckert-Gaudig, V. Pichot, D. Spitzer, V. Deckert, *ChemPhysChem* **2017**, *18*, 175.

- [24] a) L. Isa, F. Lucas, R. Wepf, E. Reimhult, *Nat. Commun.* **2011**, *2*, 438; b) D. Lee, D. A. Weitz, *Adv. Mater.* **2008**, *20*, 3498.
- [25] a) T. Higuchi, A. Tajima, H. Yabu, M. Shimomura, *Soft Matter* **2008**, *4*, 1302; b) T. Higuchi, K. Motoyoshi, H. Sugimori, H. Jinnai, H. Yabu, M. Shimomura, *Soft Matter* **2012**, *8*, 3791; c) H. Fan, Z. Jin, *Soft Matter* **2014**, *10*, 2848; d) T. Serizawa, S. Takehara, M. Akashi, *Macromolecules* **2000**, *33*, 1759.
- [26] H.-J. Butt, B. Cappella, M. Kappl, *Surf. Sci. Rep.* **2005**, *59*, 1.
- [27] C. A. Amo, R. Garcia, *ACS Nano* **2016**, *10*, 7117.
- [28] W. F. Heinz, J. H. Hoh, *Trends Biotechnol.* **1999**, *17*, 143.
- [29] a) K. K. Ray, H. D. Lee, M. A. Gutierrez, F. J. Chang, A. V. Tivanski, *Anal. Chem.* **2019**, *91*, 7621; b) M. Lorenzoni, L. Evangelio, S. Verhaeghe, C. Nicolet, C. Navarro, F. Pérez-Murano, *Langmuir* **2015**, *31*, 11630; c) A. Voss, R. W. Stark, C. Dietz, *Macromolecules* **2014**, *47*, 5236; d) T. J. Young, M. A. Monclus, T. L. Burnett, W. R. Broughton, S. L. Ogin, P. A. Smith, *Meas. Sci. Technol.* **2011**, *22*, 125703; e) P. Schön, K. Bagdi, K. Molnár, P. Markus, B. Pukánszky, G. Julius Vancso, *Eur. Polym. J.* **2011**, *47*, 692.
- [30] D. Guo, J. Li, G. Xie, Y. Wang, J. Luo, *Langmuir* **2014**, *30*, 7206.
- [31] X. Meng, H. Zhang, J. Song, X. Fan, L. Sun, H. Xie, *Nat. Commun.* **2017**, *8*, 1944.
- [32] a) Y. F. Dufrêne, T. Ando, R. Garcia, D. Alsteens, D. Martinez-Martin, A. Engel, C. Gerber, D. J. Müller, *Nat. Nanotechnol.* **2017**, *12*, 295; b) A. Bestembayeva, A. Kramer, A. A. Labokha, D. Osmanović, I. Liashkovich, E. V. Orlova, I. J. Ford, G. Charras, A. Fassati, B. W. Hoogenboom, *Nat. Nanotechnol.* **2015**, *10*, 60; c) C. Formosa-Dague, P. Speziale, T. J. Foster, J. A. Geoghegan, Y. F. Dufrêne, *Proc. Natl. Acad. Sci. USA* **2016**, *113*, 410; d) C. Heu, A. Berquand, C. Elie-Caille, L. Nicod, *J. Struct. Biol.* **2012**, *178*, 1; e) F. Rico, L. Gonzalez, I. Casuso, M. Puig-Vidal, S. Scheuring, *Science* **2013**, *342*, 741; f) G. Pletikapić, A. Berquand, T. M. Radić, V. Svetličić, *J. Phycol.* **2012**, *48*, 174; g) K. Majzner, S. Tott, L. Roussille, V. Deckert, S. Chlopicki, M. Baranska, *Analyst* **2018**, *143*, 970.
- [33] G. Mabilieu, C. Cincu, M. F. Baslé, D. Chappard, *J. Raman Spectrosc.* **2008**, *39*, 767.
- [34] K. Miyake, N. Satomi, S. Sasaki, *Appl. Phys. Lett.* **2006**, *89*, 031925.
- [35] G. Zeng, K. Dirscherl, J. Garnæs, *Nanomaterials* **2018**, *8*, 616.
- [36] E. K. Dimitriadis, F. Horkay, J. Maresca, B. Kachar, R. S. Chadwick, *Biophys. J.* **2002**, *82*, 2798.
- [37] N. Gavara, R. S. Chadwick, *Nat. Nanotechnol.* **2012**, *7*, 733.
- [38] P. D. Garcia, R. Garcia, *Biophys. J.* **2018**, *114*, 2923.
- [39] W. Megone, N. Roohpour, J. E. Gautrot, *Sci. Rep.* **2018**, *8*, 6780.